The application of a high–order discontinuous Galerkin time–domain method for the computation of electromagnetic resonant modes

Mark Dawson, Ruben Sevilla*, Kenneth Morgan

Zienkiewicz Centre for Computational Engineering, College of Engineering
Swansea University, Swansea, SA1 8EN, Wales, UK

Abstract

This work presents a highly accurate and efficient methodology for the computation of electromagnetic resonant frequencies and their associated modes in cavities. The proposed technique consists of a high–order discontinuous Galerkin time–domain solver combined with a signal processing algorithm for extracting the frequency content. The methodology is capable of incorporating the CAD boundary representation of the domain. The numerical results demonstrate that incorporating the exact boundary representation results in a improved convergence rate, a phenomenon that has not been previously reported. Several numerical examples in two and three dimensions show the potential of the proposed technique for cavities filled with non–dispersive or dispersive media.

Keywords: Maxwell's equations, resonant modes, high–order, discontinuous Galerkin, time–domain

1. Introduction

The computation of the resonant frequencies of oscillation and their associated eigenmodes is of great interest in many areas of science and engineering, including structural analysis, acoustics and electromagnetics. In the design and

*Corresponding author
Email address: r.sevilla@swansea.ac.uk (Ruben Sevilla)

characterisation of many electromagnetic devices, such as optical fibres, biological sensors, add/drop filters or photonic bandgap devices, the accurate and efficient computation of the resonant frequencies and modes of cavities is required.

The methodologies used to compute the electromagnetic resonant frequencies in cavities can be classified into frequency or time–domain solvers according to the approach utilised to solve Maxwell's equations.

Frequency domain solvers assume a time–harmonic variation of the fields and result in the need to solve a large generalised eigenvalue problem [1, 2]. The application to complex three dimensional cavities can result in prohibitively expensive computations due to the large memory requirements or due to the lack of a preconditioners suitable for the large sparse linear systems that are encountered [3, 4, 5]. In addition, the performance of the solver is strongly problem dependent. For instance, a solver designed for the solution of the eigenvalue problem arising from an electromagnetic problem with lossless materials can perform poorly when applied to problems involving loss and/or dispersive materials.

An alternative approach involves solving the problem directly in the time–domain. In this case the transient Maxwell's equations are solved using a time–domain solver and the fields are recorded at spatial points to extract the frequency content using signal processing algorithms [6]. This alternative induces significantly lower memory requirements compared to frequency domain solvers, enabling the computation of resonant modes associated with high frequencies in complex three dimensional cavities.

Among all the possible methodologies to solve the Maxwell's equations in the time–domain, the Yee scheme [7] proposed five decades ago remains the predominant technique in commercial and research software, partially due to its implementation simplicity and its low operation count for a given number of degrees of freedom. However, it is well known that this finite difference time–domain (FDTD) method requires, in its simplest form, the use of structured meshes, compromising its application to complex devices involving curved geometries.

Unstructured mesh methods such as the finite element time–domain method or the finite volume time–domain method [8] offer greater geometric flexibility but the linear approximation of curved boundaries, can create non–physical diffraction effects, especially for high–frequency problems. In addition the low order approximation of the solution is known to introduce significant dissipation and dispersion errors that become sizeable when the waves are to be propagated over long periods of time. High–order methods have emerged as a promising alternative to alleviate these issues [9]. High–order finite element techniques enable the incorporation of an accurate representation of curved geometries [10, 11] and reduce the levels of numerical dispersion and dissipation [12], a crucial aspect when the resonant frequencies are of interest. Among all the possible high–order methods, the high–order discontinuous Galerkin (DG) time–domain method has generated significant interest [13, 14, 15, 16, 17].

This work proposes a combination of the high–order DG time–domain method with a signal processing algorithm for the efficient computation of resonant frequencies in cavities. The proposed technique is able to compute a broad range of resonant frequencies and their associated modes with high accuracy. The effect of the geometric representation of cavities with curved boundaries is studied using a numerical example and it is found that the isoparametric representation traditionally used in the DG method can degrade not only the accuracy of the computed frequencies but, more importantly, the asymptotic rate of convergence. The simulations include cavities with dispersive materials and three dimensional examples.

The remainder of the paper is organised as follows. Section 2 recalls the conservative form of Maxwell's equations for both non–dispersive and dispersive materials modelled using a single–pole Drude model. The DG weak formulation of the problem is presented in Section 3. Two techniques to perform the spatial discretisation are presented in Section 4, namely the traditional isoparametric finite element method and the recently proposed NURBS–enhanced finite element method. In Section 5 the technique to compute the resonant frequencies and their associated modes from time–domain simulations is described and sev-

eral numerical examples are presented in Section 6. The examples include two and three dimensional cavities. Numerical studies confirm the optimal rate of convergence of the error on the computed resonant frequencies and the influence of the geometric approximation in the asymptotic rate of convergence is shown. Finally, Section 7 summarises the main conclusions of the work that has been presented.

2. Transient Maxwell's curl equations in dispersive media

Maxwell's curl equations in a homogeneous and isotropic lossless medium can be written as

$$\frac{\partial \tilde{\boldsymbol{B}}}{\partial \tilde{t}} + \nabla \times \tilde{\boldsymbol{E}} = \boldsymbol{0}$$
$$\frac{\partial \tilde{\boldsymbol{D}}}{\partial \tilde{t}} - \nabla \times \tilde{\boldsymbol{H}} = \boldsymbol{0}$$

with the constitutive equations that state the relation in between the electric and magnetic flux density vectors and the electric and magnetic intensity vectors, namely $\tilde{\boldsymbol{D}}(\tilde{\boldsymbol{E}})$ and $\tilde{\boldsymbol{B}}(\tilde{\boldsymbol{H}})$.

This system of linear hyperbolic equations must be supplemented with appropriate boundary and initial conditions. For the examples considered in this paper, we assume that the boundary is a perfect electric conductor (PEC), so the tangential component of the electric field vanishes on the boundary, namely

$$\boldsymbol{n} \times \tilde{\boldsymbol{E}} = \boldsymbol{0}. \tag{1}$$

2.1. Conservative form of the Maxwell's equations in dispersive media

For a dispersive medium with no magnetic polarisation, the constitutive relations are

$$\tilde{\boldsymbol{D}}(\tilde{\boldsymbol{x}}, \tilde{t}) = \epsilon_0 \epsilon_\infty \tilde{\boldsymbol{E}}(\tilde{\boldsymbol{x}}, \tilde{t}) + \tilde{\boldsymbol{P}}(\tilde{\boldsymbol{x}}, \tilde{t}) \quad \text{and} \quad \tilde{\boldsymbol{B}}(\tilde{\boldsymbol{x}}, \tilde{t}) = \mu_0 \tilde{\boldsymbol{H}}(\tilde{\boldsymbol{x}}, \tilde{t}), \tag{2}$$

where ϵ_∞ is the electric permittivity at infinite frequency and $\tilde{\boldsymbol{P}}$ denotes the electric polarisation vector.

For the single–pole Drude model considered here [18], a mechanical model is employed to express the motion of charges as a function of the electric field, resulting in the ordinary differential equation

$$\frac{\partial^2 \tilde{\boldsymbol{P}}}{\partial \tilde{t}^2} + \tilde{\gamma} \frac{\partial \tilde{\boldsymbol{P}}}{\partial \tilde{t}} - \epsilon_0 \tilde{w}_p^2 \tilde{\boldsymbol{E}} = \boldsymbol{0}, \tag{3}$$

that relates $\tilde{\boldsymbol{E}}$ and $\tilde{\boldsymbol{P}}$, where $\tilde{\gamma}$ is the electron damping coefficient and $\tilde{w}_p$ is the plasma frequency.

The approach considered here consists of introducing the dipolar current vector $\tilde{\boldsymbol{J}}^p = \partial \tilde{\boldsymbol{P}} / \partial \tilde{t}$ as a new variable, following the so–called auxiliary differential equation (ADE) method [19, 20]. Alternative techniques for including the dispersive behaviour in time–domain simulations include the recursive convolution method [21, 22] and the Z–transform method [23].

The transient Maxwell's curl equations, governing the propagation of electromagnetic waves in a dispersive lossless single–pole Drude medium with no magnetic polarisation, can be written in the differential dimensionless conservative form as

$$\frac{\partial \boldsymbol{U}}{\partial t} + \frac{\partial \boldsymbol{F}_k(\boldsymbol{U})}{\partial x_k} = \boldsymbol{S}(\boldsymbol{U}) \qquad k = 1, \ldots, \mathtt{n_{sd}} \tag{4}$$

where $\mathtt{n_{sd}}$ denote the number of spatial dimensions and, in three dimensions, the unknown vector $\boldsymbol{U}$ is given by

$$\boldsymbol{U} = \left(\epsilon_\infty E_1, \epsilon_\infty E_2, \epsilon_\infty E_3, H_1, H_2, H_3, J_1^p, J_2^p, J_3^p \right)^T, \tag{5}$$

the hyperbolic fluxes $\boldsymbol{F}_k$ are defined as

$$\begin{aligned}
\boldsymbol{F}_1 &= \Big(0, H_3, -H_2, 0, -E_3, E_2, 0, 0, 0\Big)^T, \\
\boldsymbol{F}_2 &= \Big(-H_3, 0, H_1, E_3, 0, -E_1, 0, 0, 0\Big)^T, \\
\boldsymbol{F}_3 &= \Big(H_2, -H_1, 0, -E_2, E_1, 0, 0, 0, 0\Big)^T,
\end{aligned}$$

and the source term is given by

$$\boldsymbol{S} = \Big(-J_1^p, -J_2^p, -J_3^p, 0, 0, 0, \omega_p^2\, E_1 - \gamma J_1^p, \omega_p^2\, E_2 - \gamma J_2^p, \omega_p^2\, E_3 - \gamma J_3^p\Big)^T. \quad (6)$$

The relation between the original variables (denoted by a tilde) and the dimensionless variables is

$$\boldsymbol{x} = \frac{\tilde{x}}{l}, \quad t = \frac{\tilde{t}}{l\sqrt{\epsilon_0\mu_0}}, \quad \boldsymbol{E} = \tilde{\boldsymbol{E}}, \quad \boldsymbol{H} = \sqrt{\frac{\epsilon_0}{\mu_0}}\tilde{\boldsymbol{H}}, \quad (7)$$

plus the relation for the two additional parameters introduced by the dispersive model given by

$$\omega_p = l\sqrt{\epsilon_0\mu_0}\tilde{\omega}_p, \quad \gamma = l\sqrt{\epsilon_0\mu_0}\tilde{\gamma}, \quad (8)$$

with l being a characteristic length.

It is worth mentioning that Maxwell's equations in a non–dispersive medium can be recovered from the equations in a dispersive Drude media by setting $\boldsymbol{J}^p = \boldsymbol{0}$ and $\omega_p = 0$.

2.2. Linear form of the Maxwell's equations in dispersive media

Maxwell's equations, both in non–dispersive and dispersive Drude media, form a linear hyperbolic system of equations. They can be written in the form

$$\frac{\partial \boldsymbol{U}}{\partial t} + \boldsymbol{A}_k \frac{\partial \boldsymbol{U}}{\partial x_k} = \boldsymbol{A}_s \boldsymbol{U} \qquad k = 1, \ldots, \mathtt{n_{sd}} \quad (9)$$

where, in three dimensions,

$$\boldsymbol{A}_k = \begin{pmatrix} \mathbf{0}_3 & \boldsymbol{R}_k & \mathbf{0}_3 \\ -\boldsymbol{R}_k & \mathbf{0}_3 & \mathbf{0}_3 \\ \mathbf{0}_3 & \mathbf{0}_3 & \mathbf{0}_3 \end{pmatrix}, \quad \boldsymbol{A}_s = \begin{pmatrix} \mathbf{0}_3 & \mathbf{0}_3 & -\boldsymbol{I}_3 \\ \mathbf{0}_3 & \mathbf{0}_3 & \mathbf{0}_3 \\ \omega_p \boldsymbol{I}_3 & \mathbf{0}_3 & -\gamma \boldsymbol{I}_3 \end{pmatrix}, \tag{10}$$

with

$$\boldsymbol{R}_1 = \begin{pmatrix} 0 & 0 & 0 \\ 0 & 0 & 1 \\ 0 & -1 & 0 \end{pmatrix}, \quad \boldsymbol{R}_2 = \begin{pmatrix} 0 & 0 & -1 \\ 0 & 0 & 0 \\ 1 & 0 & 0 \end{pmatrix}, \quad \boldsymbol{R}_3 = \begin{pmatrix} 0 & 1 & 0 \\ -1 & 0 & 0 \\ 0 & 0 & 0 \end{pmatrix}. \tag{11}$$

3. Discontinuous Galerkin formulation

Let us consider an open bounded domain $\Omega \subset \mathbb{R}^{\mathtt{n_{sd}}}$ with PEC boundary $\partial\Omega$ and assume that Ω is partitioned in $\mathtt{n_{el}}$ disjoint elements Ω_i, namely

$$\overline{\Omega} = \bigcup_{i=1}^{\mathtt{n_{el}}} \overline{\Omega}_i, \quad \Omega_i \cap \Omega_j = \emptyset \text{ for } i \neq j. \tag{12}$$

The DG weak formulation of Equation (4) may be expressed over a generic element Ω_e as: find $(\boldsymbol{E}, \boldsymbol{H}, \boldsymbol{J}^p) \in \mathcal{C}([0,T], \boldsymbol{\mathcal{V}})$, such that

$$\int_{\Omega_e} \boldsymbol{W} \cdot \frac{\partial \boldsymbol{U}_e}{\partial t} \mathrm{d}\Omega - \int_{\Omega_e} \frac{\partial \boldsymbol{W}}{\partial x_k} \cdot \boldsymbol{F}_k(\boldsymbol{U}_e) \mathrm{d}\Omega + \int_{\Gamma_e} \boldsymbol{W} \cdot \boldsymbol{F}_{\boldsymbol{n}}(\boldsymbol{U}_e) \mathrm{d}\Gamma = \int_{\Omega_e} \boldsymbol{W} \cdot \boldsymbol{S}(\boldsymbol{U}_e) \tag{13}$$

for all $\boldsymbol{W} \in \boldsymbol{\mathcal{V}}$, where $\boldsymbol{\mathcal{V}} = \boldsymbol{\mathcal{H}}_0(\mathbf{curl}, \Omega) \times \boldsymbol{\mathcal{H}}(\mathbf{curl}, \Omega) \times \boldsymbol{\mathcal{L}}^2(\Omega)$, with

$$\boldsymbol{\mathcal{H}}(\mathbf{curl}, \Omega) = \{\boldsymbol{v} \in \boldsymbol{\mathcal{L}}^2(\Omega) \mid \nabla \times \boldsymbol{v} \in \boldsymbol{\mathcal{L}}^2(\Omega)\}, \tag{14}$$

$$\boldsymbol{\mathcal{H}}_0(\mathbf{curl}, \Omega) = \{\boldsymbol{v} \in \boldsymbol{\mathcal{H}}(\mathbf{curl}, \Omega) \mid \boldsymbol{v} \times \boldsymbol{n} = \mathbf{0} \text{ on } \partial\Omega\} \tag{15}$$

and $\boldsymbol{\mathcal{L}}^2(\Omega) = [\mathcal{L}^2(\Omega)]^{\mathtt{n_{sd}}}$. Furthermore, in Equation (13), $\boldsymbol{U}_e$ denotes the restriction of $\boldsymbol{U}$ to the element Ω_e, $\boldsymbol{n}$ is the outward unit normal vector to the boundary Γ_e of Ω_e and $\boldsymbol{F}_{\boldsymbol{n}} = \boldsymbol{F}_k n_k$ is the normal flux on Γ_e. As usual in a DG context, the discontinuous nature of the approximation is accounted for by re-

placing the physical normal flux at the boundary by a consistent numerical flux, $\widetilde{\boldsymbol{F}}_{\boldsymbol{n}}(\boldsymbol{U}_e, \boldsymbol{U}^{\text{out}})$, that depends on both the trace of the solution at the element Ω_e, namely $\boldsymbol{U}_e$, and the trace of the solution at the neighbouring element, namely $\boldsymbol{U}^{\text{out}}$. A natural choice, for the linear hyperbolic system of interest here, is to employ a flux splitting technique, which corresponds to an upwind approximation [24]. The normal flux $\boldsymbol{F}_{\boldsymbol{n}}$ is decomposed into incoming flux (superscript $-$) and outgoing flux (superscript $+$)

$$\boldsymbol{F}_{\boldsymbol{n}}(\boldsymbol{U}_e) = \boldsymbol{F}_{\boldsymbol{n}}^{-}(\boldsymbol{U}_e) + \boldsymbol{F}_{\boldsymbol{n}}^{+}(\boldsymbol{U}_e) \tag{16}$$

where the incoming and outgoing fluxes are associated with the negative and positive eigenvalues of the Jacobian matrix $\boldsymbol{A}_{\boldsymbol{n}} = \frac{\partial \boldsymbol{F}_{\boldsymbol{n}}}{\partial \boldsymbol{U}}$ respectively. The numerical flux is then computed as

$$\widetilde{\boldsymbol{F}}_{\boldsymbol{n}}(\boldsymbol{U}_e, \boldsymbol{U}^{\text{out}}) = \boldsymbol{F}_{\boldsymbol{n}}^{+}(\boldsymbol{U}_e) + \boldsymbol{F}_{\boldsymbol{n}}^{-}(\boldsymbol{U}^{\text{out}}) \tag{17}$$

Introducing the resulting numerical normal flux into equation (13), the DG weak formulation for element Ω_e can be re–written as

$$\int_{\Omega_e} \boldsymbol{W} \cdot \frac{\partial \boldsymbol{U}_e}{\partial t} \mathrm{d}\Omega + \int_{\Omega_e} \boldsymbol{W} \cdot \frac{\partial \boldsymbol{F}_k(\boldsymbol{U}_e)}{\partial x_k} \mathrm{d}\Omega + \int_{\Gamma_e} \boldsymbol{W} \cdot \boldsymbol{A}_n^{-} [\![\boldsymbol{U}_e]\!] \mathrm{d}\Gamma = \int_{\Omega_e} \boldsymbol{W} \cdot \boldsymbol{S}(\boldsymbol{U}_e) \tag{18}$$

where $[\![\boldsymbol{U}_e]\!] = \boldsymbol{U}_e - \boldsymbol{U}^{\text{out}}$ denotes the jump in the solution across Γ_e and the boundary term, is given by

$$\boldsymbol{A}_n^{-} [\![\boldsymbol{U}]\!] = \frac{1}{2} \begin{pmatrix} -\boldsymbol{n} \times [\![\boldsymbol{H}]\!] + \boldsymbol{n} \times (\boldsymbol{n} \times [\![\boldsymbol{E}]\!]) \\ \boldsymbol{n} \times [\![\boldsymbol{E}]\!] + \boldsymbol{n} \times (\boldsymbol{n} \times [\![\boldsymbol{H}]\!]) \\ \mathbf{0}_{\mathrm{n_{sd}} \times 1} \end{pmatrix}. \tag{19}$$

At an inter–element boundary, the jump of the solution is computed using the traces of the solution at the current and neighbouring elements. In contrast, for a face on the PEC boundary, condition (1) only specifies the tangential component of the electric field. As usual in the framework of hyperbolic equations,

the Rankine–Hugoniot jump conditions must be employed to determine the unknown conditions. At a PEC boundary, the resulting expression of the boundary term is

$$\boldsymbol{A}_n^- [\![\boldsymbol{U}]\!] = \begin{pmatrix} \boldsymbol{n} \times (\boldsymbol{n} \times \boldsymbol{E}) \\ \boldsymbol{n} \times \boldsymbol{E} \\ \boldsymbol{0}_{\mathtt{n_{sd}} \times 1} \end{pmatrix}. \tag{20}$$

Convergence of the DG method for the system of Maxwell's equations in a Drude dispersive medium bounded by a PEC has been recently proved [25].

4. Spatial discretisation

This section describes two approaches to perform the spatial discretisation of the weak formulation (18), namely the traditional isoparametric finite element formulation and the recently proposed NURBS–enhanced finite element method (NEFEM).

4.1. Isoparametric finite element method

A nodal interpolation of the solution, $\boldsymbol{U}$, is defined in a reference element $\widehat{\Omega}$, with local coordinates $\boldsymbol{\xi}$, as

$$\boldsymbol{U}(\boldsymbol{\xi}, t) \simeq \boldsymbol{U}_h(\boldsymbol{\xi}, t) = \sum_{j=1}^{\mathtt{n_{en}}} \mathbf{U}_j(t) N_j(\boldsymbol{\xi}) \tag{21}$$

where $\mathbf{U}_j$ denote the (time–dependent) nodal values, N_j are polynomial shape functions of order p in $\boldsymbol{\xi}$ and $\mathtt{n_{en}}$ is the number of nodes per element. Then, the isoparametric transformation is used to link the reference element $\widehat{\Omega}$ with a generic mesh element Ω_e^h, namely

$$\boldsymbol{\phi}(\boldsymbol{\xi}) = \sum_{j=1}^{\mathtt{n_{en}}} \boldsymbol{x}_j N_j(\boldsymbol{\xi}) \tag{22}$$

where $\boldsymbol{x}_j$ are the nodal coordinates of the element Ω_e^h and N_j are the same polynomial shape functions of order p used for the interpolation in Equation (21). It

is important to remark that, for an element with a face or edge on the boundary of the computational domain, the boundary of the element Ω_e^h is a polynomial approximation of order p of the true boundary [10].

Introducing the approximate solution (21) into the weak form of equation (19) and selecting the space of weighting or test functions to be the same as the space spanned by the approximation functions, the system

$$\sum_{j=1}^{\mathtt{n_{en}}} \mathbf{M}_{ij} \boldsymbol{I} \frac{d\mathbf{U}_j}{dt} + \sum_{j=1}^{\mathtt{n_{en}}} \left(\mathbf{C}_{ij}^k \boldsymbol{A}_k \right) \mathbf{U}_j - \sum_{j=1}^{\mathtt{n_{fn}}} \mathbf{m}_{ij} \boldsymbol{A}_n^- [\![\mathbf{U}_j]\!] = \sum_{j=1}^{\mathtt{n_{en}}} \mathbf{M}_{ij} \boldsymbol{A}_s \mathbf{U}_j \tag{23}$$

of ordinary differential equations is obtained for every node i of element Ω_e^h. Here, $\mathbf{M}$ denotes the elemental mass matrix, $\mathbf{C}^k$ the elemental convection matrix in the x_k direction, $\mathbf{m}$ is the face mass matrix, $\boldsymbol{I}$ is the identity matrix and $\mathtt{n_{fn}}$ is the number of nodes per face. These matrices are defined by

$$\mathbf{M}_{ij} = \int_{\Omega_e^h} N_i N_j \mathrm{d}\Omega, \quad \mathbf{C}_{ij}^k = \int_{\Omega_e^h} N_i \frac{\partial N_j}{\partial x_k} \mathrm{d}\Omega \quad \text{and} \quad \mathbf{m}_{ij} = \int_{\Gamma_e^h} N_i N_j \mathrm{d}\Gamma. \tag{24}$$

Using the isoparametric mapping (22), the integrals over element Ω_e^h are evaluated on a reference element, $\widehat{\Omega}$ as

$$\mathbf{M}_{ij} = \int_{\widehat{\Omega}} N_i N_j |\boldsymbol{J}| \mathrm{d}\Omega \quad \text{and} \quad \mathbf{C}_{ij}^k = \int_{\widehat{\Omega}} N_i \left(\sum_{l=1}^{\mathtt{n_{sd}}} \boldsymbol{J}_{kl}^{-1} \frac{\partial N_j}{\partial \xi_l} \right) |\boldsymbol{J}| \mathrm{d}\Omega \tag{25}$$

where $\boldsymbol{J} = \partial \boldsymbol{\phi} / \partial \boldsymbol{\xi}$ is the Jacobian of the isoparametric transformation. Similarly, the face mass matrix is evaluated as

$$\mathbf{m}_{ij} = \int_{\widehat{\Gamma}} N_i N_j \| \boldsymbol{J}^f \| \mathrm{d}\Gamma \tag{26}$$

where $\boldsymbol{J}^f$ is the Jacobian of the restriction of the isoparametric mapping to the element face f.

4.2. NURBS–enhanced finite element method (NEFEM)

The isoparametric mapping induces a geometric approximation of curved boundaries, which can have a non–negligible impact in some applications [10]. The recently proposed NEFEM completely removes the geometric uncertainty induced by a polynomial approximation of curved boundaries. In this case, the CAD boundary representation of the domain given by NURBS curves or surfaces is considered [26].

In a NEFEM context [26], the approximation is defined directly in the physical space, with Cartesian coordinates, namely

$$\boldsymbol{U}(\boldsymbol{x},t) \simeq \widetilde{\boldsymbol{U}}_h(\boldsymbol{x},t) = \sum_{j=1}^{\mathtt{n}_{\mathtt{en}}} \widetilde{\mathbf{U}}_j(t)\widetilde{N}_j(\boldsymbol{x}) \tag{27}$$

where $\widetilde{\mathbf{U}}_j$ denote the (time–dependent) nodal values and $\widetilde{N}_j$ are polynomial shape functions of order p in $\boldsymbol{x}$.

Introducing the approximate solution (27) into the weak form of equation (19) and selecting the space of weighting or test functions to be the same as the space spanned by the approximation functions, the system of ordinary differential equations

$$\sum_{j=1}^{\mathtt{n}_{\mathtt{en}}} \widetilde{\mathbf{M}}_{ij}\boldsymbol{I}\frac{d\widetilde{\mathbf{U}}_j}{dt} + \sum_{j=1}^{\mathtt{n}_{\mathtt{en}}} \left(\widetilde{\mathbf{C}}_{ij}^k \boldsymbol{A}_k\right)\widetilde{\mathbf{U}}_j - \sum_{j=1}^{\mathtt{n}_{\mathtt{en}}} \widetilde{\mathbf{m}}_{ij}\boldsymbol{A}_n^-[\![\widetilde{\mathbf{U}}_j]\!] = \sum_{j=1}^{\mathtt{n}_{\mathtt{en}}} \widetilde{\mathbf{M}}_{ij}\boldsymbol{A}_s\widetilde{\mathbf{U}}_j \tag{28}$$

is obtained for every node i of element Ω_e, where the elemental matrices are given by

$$\widetilde{\mathbf{M}}_{ij} = \int_{\Omega_e} \widetilde{N}_i\widetilde{N}_j \mathrm{d}\Omega, \quad \widetilde{\mathbf{C}}_{ij}^k = \int_{\Omega_e} \widetilde{N}_i\frac{\partial \widetilde{N}_j}{\partial x_k}\mathrm{d}\Omega \quad \text{and} \quad \widetilde{\mathbf{m}}_{ij} = \int_{\Gamma_e} \widetilde{N}_i\widetilde{N}_j \mathrm{d}\Gamma. \tag{29}$$

The main differences between NEFEM and isoparametric elements are

- NEFEM ensures that the geometry is exactly represented, irrespective of the mesh used, whereas in isoparametric FEM the mesh introduces a geometric approximation. The integrals in Equation (29) are defined over

Ω_e and Γ_e whereas integrals in Equation (24) are defined over Ω_e^h and Γ_e^h.

- Isoparametric elements define the approximation in a reference element, with local coordinates ($\boldsymbol{\xi}$), whereas NEFEM defines the approximation directly in the physical space, with Cartesian coordinates ($\boldsymbol{x}$) [27, 11]. Therefore NEFEM ensures the reproducibility of polynomials in the physical space whereas this is not guaranteed for isoparametric FEM. This difference induces the different notation used for the approximation in Equations (21) and (27). This change also implies that the summation in Equation (28) corresponding to the face integral contains all element nodes, rather than only the face nodes as in the isoparametric approach described in Equation (23).

- The numerical integration in the isoparametric FEM is performed over a reference element. NEFEM uses specifically designed numerical quadratures that account for the exact boundary representation given by a CAD model [28].

Remark 1. *Super-parametric finite elements are an alternative to improve the geometric representation of isoparametric elements [29]. This approach consists of using a higher polynomial representation for the geometry of the computational domain, viz. Equation (21), than for the functional approximation, viz Equation (22). This approach has not been considered in the present work because the implementation effort required and the computational cost is similar to NEFEM but its accuracy is always lower due to the use of a polynomial representation of the boundary of the computational domain. A comparison of isoparametric, super-parametric and NEFEM elements can be found in [30].*

4.3. Computational aspects

The implementation considered in this work employs the optimal interpolation points proposed in [31] and the technique proposed in [13] for constructing high–order polynomial basis function. The quadratures employed to integrate

the terms of the weak form correspond to the integration rules recently proposed in [32]. The number of integration points is selected so that exact integration is achieved for polynomials of order less than or equal to $2p+1$.

The meshes used in this work are designed to maximise the number of elements where an affine mapping can be established between the physical and reference elements. As shown in [33], the cost of a high–order DG method can be reduced by a factor of 100 by using a quadrature–free implementation [34]. For instance, the mass matrix can be computed once in the reference element and, for each element, the computation of an elemental mass matrix reduces to a multiplication of a scalar by the matrix of the reference element, namely

$$\mathbf{M}_{ij} = |\boldsymbol{J}| \int_{\widehat{\Omega}} N_i N_j d\Omega = |\boldsymbol{J}| \hat{\mathbf{M}}_{ij}, \tag{30}$$

thus avoiding the loop over integration points in each time step.

High–order curvilinear meshes for the isoparametric FEM are obtained using the solid mechanics analogy proposed in [35, 36], whereas the meshes for NEFEM are generated using the technique recently proposed in [37]. For curved elements, it is not possible to precompute the mass matrix in the reference element and scale it with the Jacobian for each physical element. Due to the extremely low number of curved elements present in practical applications, it is possible to precompute the mass matrix for each curved element.

5. Computation of resonant frequencies and modes

The proposed strategy to compute the resonant frequencies and their associated modes in a cavity consist of two stages.

5.1. Computation of resonant frequencies

Resonant frequencies of a cavity are computed using a time–domain solver by integrating the Maxwell's equations in time using an initial condition or current source designed to excite the frequencies within a desired interval. The use of localised pulses designed to excite a broad range of frequencies is commonly

used [38, 18, 39], although, it is possible to exclude unwanted frequencies by carefully exciting the fields [40]. In all the numerical examples considered here, the initial condition corresponds to

$$U_1(x,0) = U_2(x,0) = 0, \quad \forall \boldsymbol{x} \in \Omega, \qquad U_3(x,0) = \begin{cases} 1 & \text{if } \boldsymbol{x} = \{\boldsymbol{x}_m\}_{m=1}^{\mathtt{n}_{\mathtt{mon}}}, \\ 0 & \text{otherwise} \end{cases} \tag{31}$$

where $\boldsymbol{x}_m$, for $m = 1, \ldots, \mathtt{n}_{\mathtt{mon}}$, denote the $\mathtt{n}_{\mathtt{mon}}$ monitor points.

The solution is then advanced using a time marching algorithm and the electromagnetic fields are recorded at one or several points. In this work an explicit fourth order Runge–Kutta scheme is employed for advancing the solution in time. When combined with the spatial DG discretisation described in the previous section, this results in an efficient and low–storage approach because the resulting mass matrix is block diagonal [33]. Figure 1(a) shows the initial condition used for the computation of the resonant frequencies in a rectangular cavity, where the red circle denotes the monitor point $\boldsymbol{x}_m$ used to record the signal. The field at $t = 0.09$ps is also depicted in Figure 1(b).

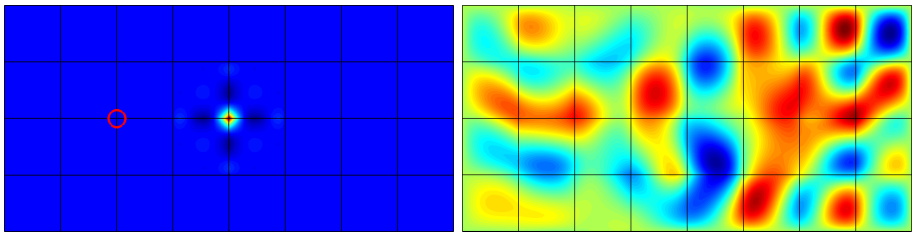

(a) $t = 0$ps (b) $t = 0.09$ps

Figure 1: Simulation of a rectangular PEC cavity showing (a) the initial condition and monitor point and (b) the field at $t = 0.09$ps.

At the end of the time–domain simulation, a signal processing algorithm is applied to the recorded fields to compute the resonant frequencies. The most popular choice is the fast Fourier transform (FFT) but other alternatives such as the filter diagonalisation method (FDM [41]) are available. In this work we use the FFT as the main interest is to study the performance of the proposed spatial

discretisation techniques. Figure 2 shows the time–domain signal recorded at the monitor point shown in Figure 1(a) and the frequency spectrum after the FFT is applied.

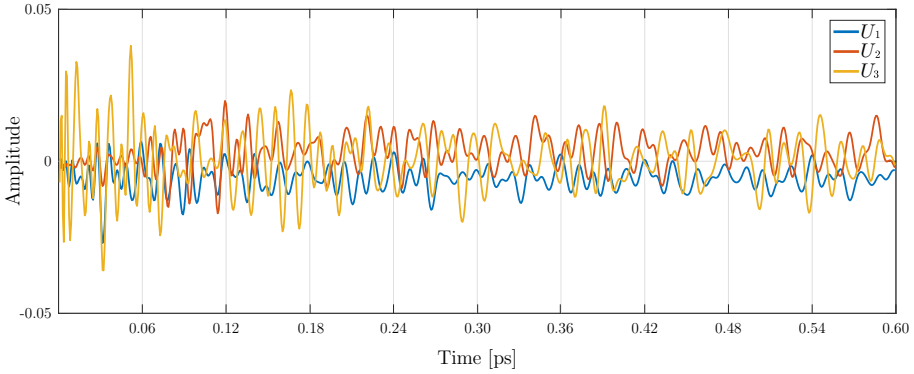

(a) Time–domain signal

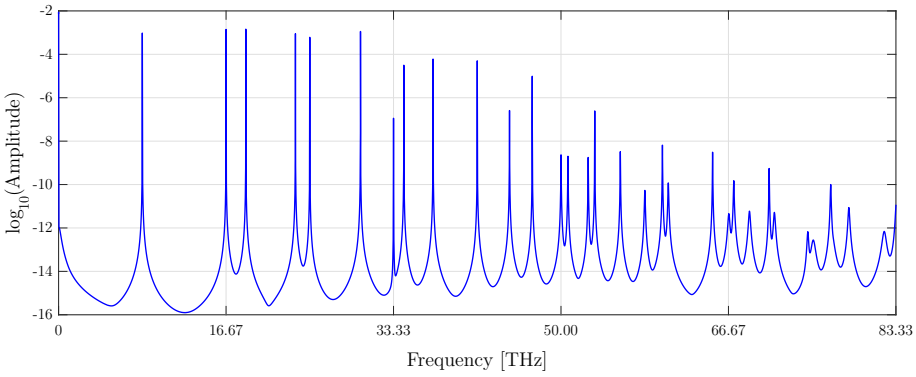

(b) Spectrum

Figure 2: Simulation of a rectangular PEC cavity showing (a) the amplitude of the fields and (b) the spectrum obtained after applying the FFT.

The choice of the monitor point/s significantly influences the final spectrum obtained. For instance, if a monitor point coincides with a symmetry point of a particular mode, the frequency associated to this mode will not be extracted when applying the signal processing algorithm to the recorded signal. This effect can be utilised to avoid exciting undesired modes [42].

Finally, it is worth mentioning that filters are commonly applied to the recorded fields to reduce spectral leakage effects induced by the finite length of

a signal. For the examples considered in this work, a Blackman filter is applied prior to extracting the frequency content [43].

5.2. Computation of resonant modes

After the resonant frequencies are computed, the associated resonant modes are obtained by performing a discrete Fourier transform (DFT) for each frequency of interest and at each point in space, namely

$$\widehat{\mathbf{U}}_j(f_k) = \sum_{n=0}^{\mathtt{n_T}-1} \mathbf{U}_j(t_n) \exp(-2\pi I t_n f_k), \quad j = 1, \cdots, \mathtt{n_{node}}, \tag{32}$$

where $\mathtt{n_T}$ is the total number of time steps, $I = \sqrt{-1}$, f_k are the computed resonant frequencies, $t_n = n\Delta t$, Δt is the time step, $\mathtt{n_{node}}$ is the total number of mesh nodes and $\widehat{\mathbf{U}}_j(f_k)$ is the complex amplitude of the mode associated to frequency f_k at node j of the mesh.

One alternative to obtain the complex amplitude of the resonant modes would involve recording the signal during the time domain simulation at all nodes of the computational mesh. After the resonant frequencies are obtained, folllowing the procedure described in Section 5.1, a direct application of Equation (32) provides the complex amplitude of each mode at all the nodes of the mesh. The main drawback of this approach is the large memory required to store all the components of the electric and magnetic fields at all points of the mesh and for each instant of the time–domain simulation.

To reduce the required memory, a second alternative, considered in this work, consists of performing a second run of the time–domain solver after the resonant frequencies are obtained. In the second run, the DFT given by Equation (32), is performed *on the fly*, during the time marching process. The extra memory of a built-in DFT is negligible as it only requires a vector, of dimension equal to the total number of mesh nodes for each component of the electric and magnetic field, to be stored. Furthermore, the extra computational cost of the built-in DFT is also negligible as it only requires performing a multiplication of a vector, containing the values of the electromagnetic fields, by a scalar, given by

the exponential in Equation (32), and accumulating the result in a vector.

6. Numerical examples

This section presents a number of numerical examples to validate the implementation of the proposed technique for both non–dispersive and dispersive materials. A comparison of the performance of low and high–order elements is presented as well as the effect of the geometric representation of cavities with curved boundaries on the accuracy and convergence properties of the proposed methodology.

In all the examples a fourth order explicit time marching scheme is considered. As the main focus here is to study the error due to the spatial discretisation, the time step is selected to be small enough to ensure that the error induced by the time marching algorithm is lower than the spatial error. Similarly, the final time is selected to be large enough to ensure the error of the FFT is lower than the spatial error.

In practice, the maximum time step is given by $\Delta t = \lceil 1/(2f_M) \rceil$, where f_M is the maximum frequency of interest and $\lceil \cdot \rceil$ denotes the ceiling function, because for a discrete signal it is necessary to have at least two sampling points per period. The final time of the time–domain simulation, T, is selected in practice as $T = 1/(\Delta f)$, where Δf is the length of the interval between two consecutive frequencies obtained from the FFT.

6.1. Rectangular non–dispersive cavity

The first example involves the computation of the resonant frequencies and associated modes on a rectangular PEC cavity of dimension $2L \times L$ where L =20μm filled with air. The objective is to show the optimal convergence of the proposed approach for approximating the resonant frequencies and compare the performance of high and low–order approximations.

The resonant frequencies are computed using a series of structured quadrilateral meshes with 4×2, 8×4, 16×8, 32×16 and 64×32 elements. Figure 3

shows the evolution of the relative error on two computed resonant frequencies as a function of the element size for a degree of approximation p ranging from 1 up to 3. In this figure, and in subsequent examples, f_i denotes the computed

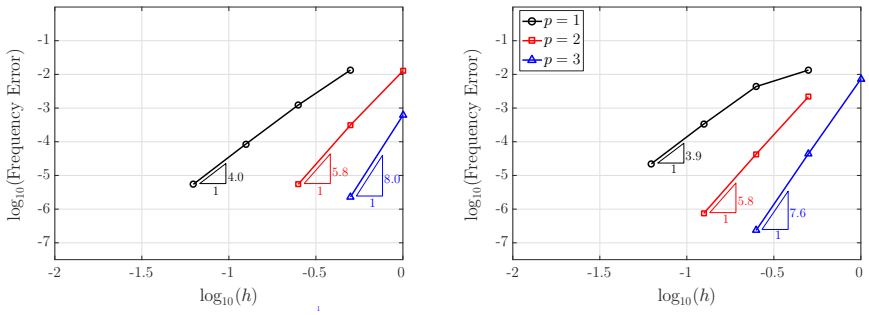

(a) $f_3 \approx 8.38$ THz (b) $f_6 \approx 13.51$ THz

Figure 3: Rectangular non–dispersive cavity: h-convergence of the relative error for two resonant frequencies.

i-th resonant frequency and the frequencies are assumed ordered from lowest to highest, i.e. $f_i < f_j$ if $i < j$. The error in the computed frequency f_i is evaluated as $\epsilon_i = (|f_i - f_i^\star|)/f_i^\star$, where $f_i^\star$ is the known exact value of the resonant frequency [44].

In all the examples, the theoretical $2p + 2$ rate of convergence [12] is approximately obtained, confirming the optimality of the proposed approach for computing the resonant frequencies of a non–dispersive cavity. It can be observed that, for a given mesh and degree of approximation, the error increases as the frequency increases, illustrating the challenge in approximating higher frequencies.

The results also illustrate the benefit of using high–order approximations. In the second mesh, the use of a cubic approximation of the solution offers a result almost four orders more accurate than using a linear approximation and two orders of magnitude more accurate than using a quadratic approximation. In the two cases presented in Figure 3, the use of a cubic approximation in the second mesh and a linear approximation in the finest mesh provide similar accuracy.

This implies that the computation with p=3 provides the same accuracy as the computation with p=1 by reducing the number of degrees of freedom by a factor of almost 20. It is worth mentioning that the required use of finer meshes with linear elements induces a significantly higher computational cost due to the use of an explicit time marching scheme.

In this numerical example, with a coarse mesh of 8×4 elements and a cubic degree of approximation, it is possible to capture resonant frequencies up to 22.49 THz with an error below 10^{-4} and resonant frequencies up to 35.98 THz with an error below 10^{-3}.

After computing the resonant frequencies, the associated modes can be extracted by performing a discrete Fourier transform as described in Section 5. Figure 4 shows the second component of the electric field for the four modes associated to the frequencies f_3, f_4, f_6 and f_9.

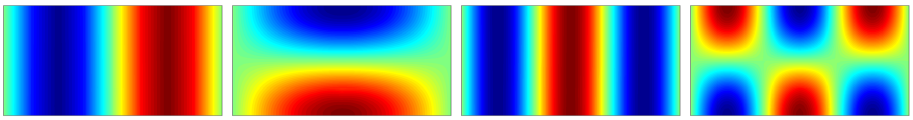

(a) $f_3 \approx 8.38$ THz (b) $f_4 \approx 10.60$ THz (c) $f_6 \approx 13.51$ THz (d) $f_9 \approx 16.76$ THz

Figure 4: Rectangular non–dispersive cavity: component E_2 of four resonant modes.

To further illustrate the potential of the proposed approach, Figure 5 shows the first electric and magnetic component of the electromagnetic field corresponding to a high frequency mode, with associated resonant frequency of $f_{26} \approx 31.80$ THz. The computation has been performed on a very coarse mesh with only 8 elements and using a degree of approximation p=4 and the the relative error of the computed modes measured in the $\mathcal{L}^2(\Omega)$ norm is 0.0135.

6.2. Effect of the geometric representation for cavities with curved boundaries

The second example considers the computation of the resonant frequencies and associated modes in a PEC disk resonator of radius 1μm filled with air, for which an analytical solution is known [44]. The objective is to study the effect of the geometric approximation of curved boundaries on the accuracy

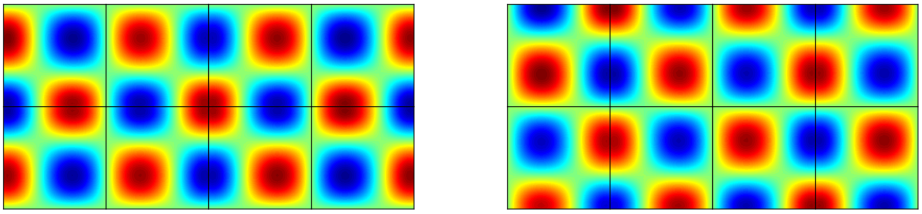

(a) E_1 (b) H_1

Figure 5: Rectangular non–dispersive cavity: two components of a high frequency resonant mode corresponding to the resonant frequency $f_{26} \approx 31.80$ THz.

and convergence properties of isoparametric finite elements and NEFEM. In addition, the benefit of using high–order curved elements in this context is quantified by comparing the computational time required to obtain the same accuracy.

The resonator is discretised using a series of unstructured triangular meshes with 4, 16, 64, 256, and 1,024 elements and with different orders of approximation. Figure 6(a) shows the evolution of the error in the first resonant frequency, $f_1 \approx 57.59$ THz, as a function of the element size for linear ($p = 1$) and quadratic elements ($p = 2$) and by using standard isoparametric finite elements and NEFEM. The results show that the geometric approximation of

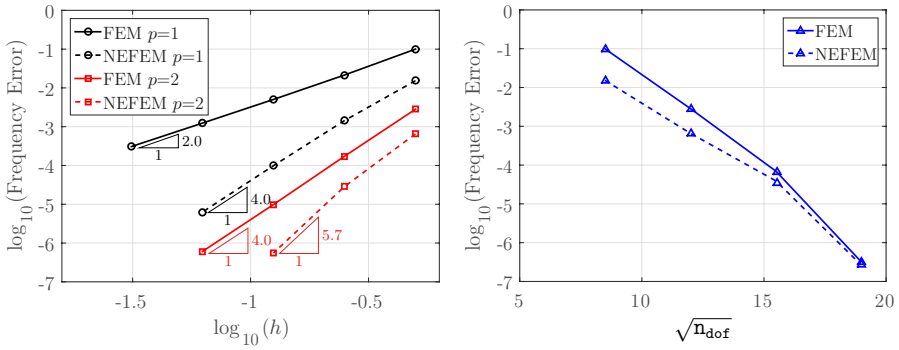

(a) h-refinement (b) p-refinement

Figure 6: Disk resonator: h-convergence and p-convergence of the error for the first resonant frequency $f_1 \approx 57.59$ THz.

curved boundaries introduced by standard finite elements induces not only a

significant loss of accuracy but, more importantly, a loss of the optimal rate of convergence. For example, in the fourth mesh, with 256 elements and using a linear approximation of the solution, the error in resonant frequency with NEFEM is more than two orders of magnitude lower than the error obtained using standard finite elements. For isoparametric finite element a rate of convergence $2p$ is observed whereas for NEFEM the optimal rate of convergence, $2p+2$, is observed. The order $2p$ corresponds to the rate of convergence of the geometric error, understood as the area between the true boundary and the approximation with polynomials of order p induced by an isoparametric approach.

Figure 6(b) shows a p-refinement study. A coarse mesh, with only four elements, is considered and the degree of approximation is increased from p=1 to p=4. The evolution of the error in the first resonant frequency, as a function of the square root of the number of degrees of freedom, is represented for both isoparametric finite elements and NEFEM. The comparison shows important differences for low order approximations (i.e, p=1,2) whereas for higher order approximations (i.e, $p \geq 3$), a similar error is obtained. These results indicate that, in the presence of curved boundaries, an accurate geometric approximation is required to compute the resonant frequencies. If an accurate geometric description is employed, the error in the computed frequency is controlled by the numerical dispersion of the scheme (of order $2p+2$) rather than being controlled by the geometric error (of order $2p$).

Figure 7 shows the third component of the electric field for twelve modes. The modes are extracted by performing a discrete Fourier transform as described in Section 5. All the modes are computed using a single time–domain run on a mesh with only 1,024 elements and using a degree of approximation p=5 (i.e, 46,080 degrees of freedom). The error in the highest computed resonant frequency ($f_{20} \approx 310.50$ THz) is less than 0.3%, illustrating the potential of the proposed approach for computing resonant frequencies and the associated modes over a broad frequency band.

Next, the performance of both low and high–order approximations is studied. Figure 8 shows the evolution in the error of the first computed resonant

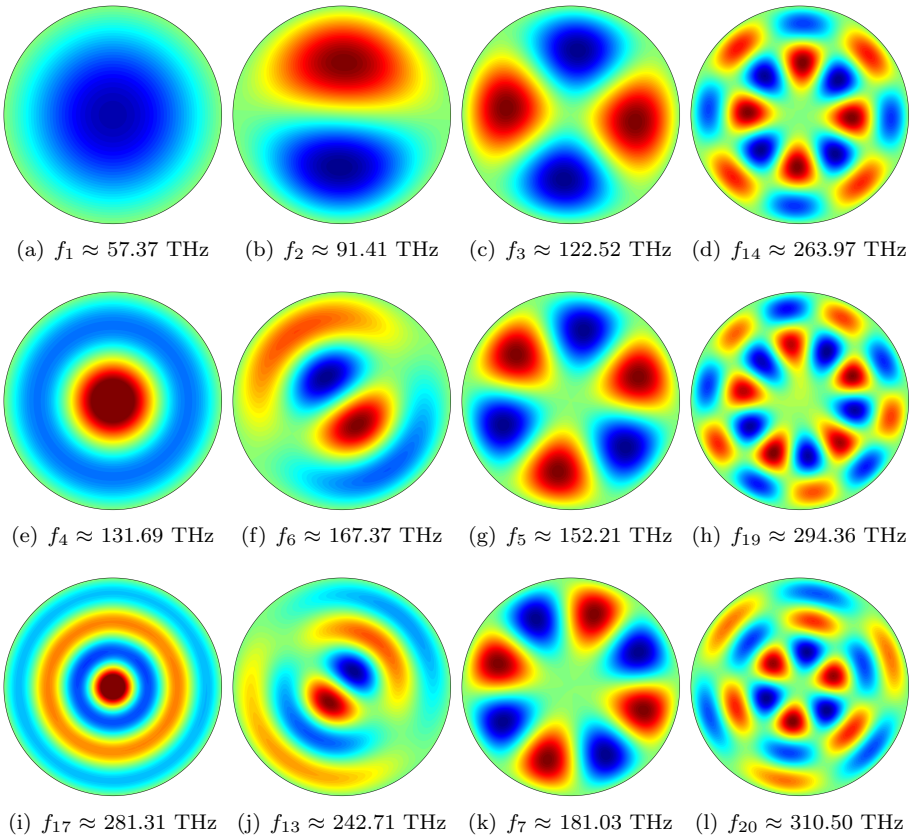

(a) $f_1 \approx 57.37$ THz (b) $f_2 \approx 91.41$ THz (c) $f_3 \approx 122.52$ THz (d) $f_{14} \approx 263.97$ THz

(e) $f_4 \approx 131.69$ THz (f) $f_6 \approx 167.37$ THz (g) $f_5 \approx 152.21$ THz (h) $f_{19} \approx 294.36$ THz

(i) $f_{17} \approx 281.31$ THz (j) $f_{13} \approx 242.71$ THz (k) $f_7 \approx 181.03$ THz (l) $f_{20} \approx 310.50$ THz

Figure 7: Disk resonator: component H_3 of twelve resonant modes.

frequency as a function of the number of degrees of freedom ($\mathtt{n_{dof}}$) and the CPU time for low and high–order approximations. In both cases NEFEM is considered in order to avoid the error introduced by the polynomial approximation of curved boundaries inherent to standard isoparametric finite elements.

Figure 8(a) shows a comparison of low and high-order approximations in terms of the memory requirements (i.e. number of degrees of freedom) to obtain a desired accuracy. For the h-refinement strategy linear approximation is considered in successively refined meshes whereas the p-refinement strategy consist on increasing the degree of approximation from $p = 1$ to $p = 4$ in the same coarse mesh. As expected, high–order elements significantly outperform

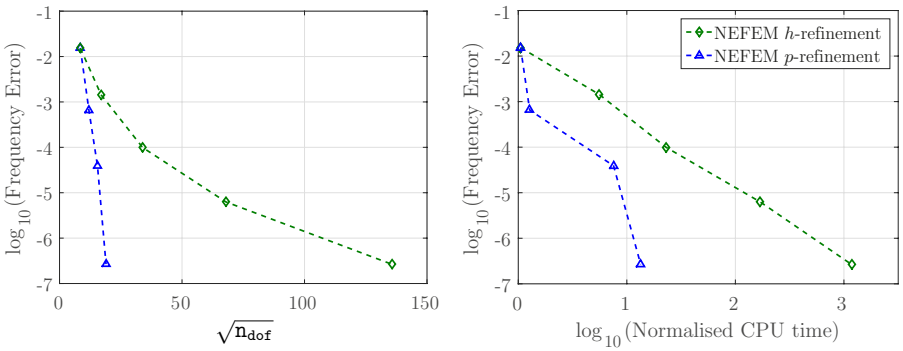

Figure 8: Disk resonator: Comparison of h and p refinement in terms of(a) the number of degrees of freedom ($\mathtt{n_{dof}}$) and(b) the CPU time for the computation of the first resonant frequency $f_1 \approx 57.59$ THz.

low–order elements, due to the exponential rate of convergence of a p-refinement strategy compared to the algebraic rate of an h-refinement strategy when the solution is smooth. In this example, for an error in the first resonant frequency of 10^{-4}, the number of degrees of freedom required using NEFEM with linear approximation is 1,149, whereas the same accuracy can be obtained using approximately 204 degrees of freedom with $p = 3$ on a coarser mesh. For higher accuracy, namely an error in the first resonant frequency of 2.5×10^{-7}, the use of high–order methods is even more advantageous. NEFEM with linear approximation requires 18,432 degrees of freedom, whereas the same accuracy can be obtained using only 360 degrees of freedom with $p = 4$ on a coarser mesh.

The reduction in number of degrees of freedom introduced by a high–order functional approximation has been consistently observed in many examples and it is a crucial factor in the growing interest in high–order methods not only within the computational electromagnetics and but also within the computational fluid dynamics community [45, 46]. In some cases this reduction is not necessarily expected to translate in a lower computational cost due to the extra computational cost per element induced by a high–order approximation. Figure 8(b) shows the comparison of low and high–order approximations in terms of the normalised CPU time (i.e, CPU time of the current simulation divided

by the CPU time of the simulation with linear elements in the coarsest mesh) on a logarithmic scale. The results demonstrate that high–order methods are not only competitive in terms of memory requirements (as discussed from the results in Figure 8(a)), but more importantly, in terms of the computing time. In this example, an error in the first resonant frequency of 10^{-4} is achieved using high–order elements 5.5 times faster than using linear elements. For higher accuracy, namely an error in the first resonant frequency of 2.5×10^{-7}, high–order elements are 88 times faster than linear elements.

It is worth noting that the speed up factor of high–order elements compared to low–order elements is similar, or even higher, than the factor by which the number of degrees of freedom is reduced, clearly illustrating the potential and performance of high–order elements for the computation of resonant frequencies in cavities. It is also worth mentioning that the superiority of high–order approximations in other electromagnetic problems where the error of the electromagnetic fields is of interest has been previously reported in [33].

6.3. Dispersive cavity

First, the implementation of the DG method for a lossless single–pole Drude medium with no magnetic polarisation is validated for a square cavity filled with a dispersive material with non–dimensional constants $\omega_p = 0.7933$ and $\gamma = 0.076$ and with a PEC boundary. A volumetric source term is considered so that the analytical solution is given by

$$\boldsymbol{E} = \sin(\pi t) \begin{pmatrix} -\cos(\pi x_1)\sin(\pi x_2) \\ \sin(\pi x_1)\cos(\pi x_2) \\ 2\sin(\pi x_1)\sin(\pi x_2) \end{pmatrix} \quad \boldsymbol{H} = \cos(\pi t) \begin{pmatrix} -\sin(\pi x_1)\cos(\pi x_2) \\ \cos(\pi x_1)\sin(\pi x_2) \\ -\cos(\pi x_1)\cos(\pi x_2) \end{pmatrix}. \tag{33}$$

The computations are performed on a series of structured triangular meshes with 2, 8, 32, 126, 556 and 2,310 elements and for a degree of approximation ranging from p=1 to p=4. Initial and boundary conditions corresponding to the analytical solution are considered. The final time corresponds to T=3 and the

time step is small enough to ensure that the error due to the time integration is lower than the error introduced by the functional approximation.

Figure 9 shows the $\mathcal{L}^2(\Omega)$ norm of the error of two components of the electromagnetic field, namely E_1 and H_3, as a function of the characteristic element size h. In all cases, the expected optimal rate of convergence (i.e, p+1) is observed.

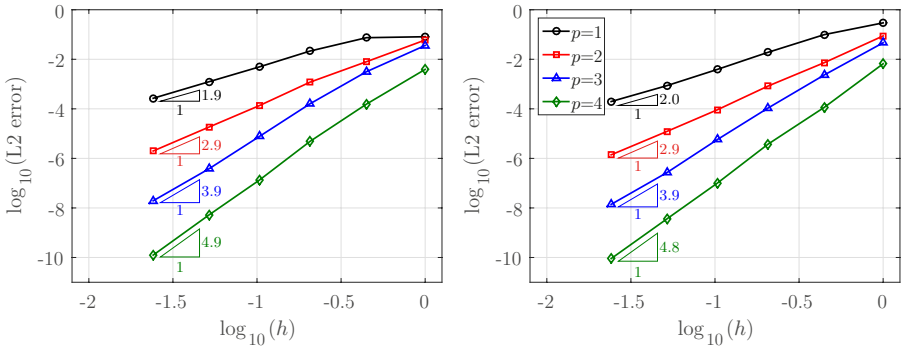

(a) E_1 (b) H_3

Figure 9: Rectangular dispersive cavity: h-convergence of the $\mathcal{L}^2(\Omega)$ norm of the error of two components of the electromagnetic field as a function of the characteristic element size h for different degrees of approximation (p).

The next example considers a rectangular cavity of dimension $2L \times L$, with L =20μm made of the same dispersive material as the previous example and with a PEC boundary. This example is used to test the convergence properties of the proposed technique for the computation of resonant frequencies in a dispersive medium. The analytical resonant frequencies can be numerically computed by computing the roots of the function as described in [44]. Figure 10 shows the evolution of the error of two computed resonant frequencies as a function of the element size for linear and quadratic elements. In all the examples, the expected $2p+2$ rate of convergence is approximately obtained, confirming the optimality of the proposed approach for computing the resonant frequencies of cavities filled with dispersive materials. As in previous examples, it can be observed that, for a given mesh and degree of approximation, the error increases as the frequency

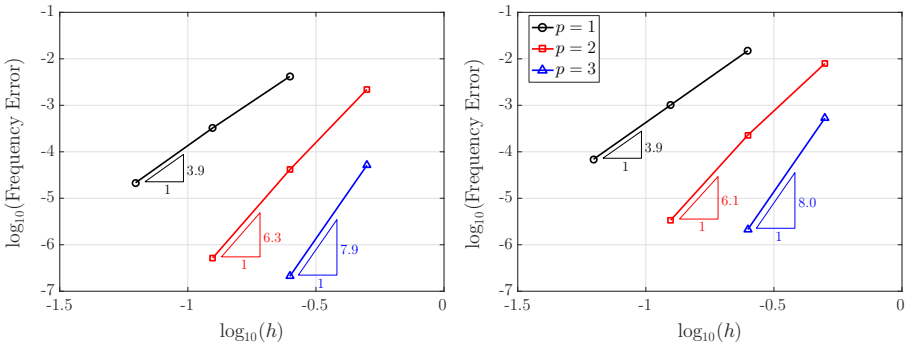

(a) $f_6 \approx 13.64$ THz (b) $f_{10} \approx 18.83$ THz

Figure 10: Rectangular dispersive cavity: h-convergence of the error for two resonant frequencies.

increases, illustrating the challenge in approximating higher frequencies.

The effect of the dispersive material on the computed spectrum can be observed in Figure 11 by comparing the spectrum for both the non–dispersive cavity and the dispersive cavity using, in both cases, a mesh with 128 elements and a degree of approximation p=2. The results reveal a shift of all the frequencies. The shift is more sizeable for low frequencies than for the higher frequencies. It can also be observed that the amplitude of the signal in the dispersive cavity is lower than the signal recorded in the cavity filled with a non–dispersive material.

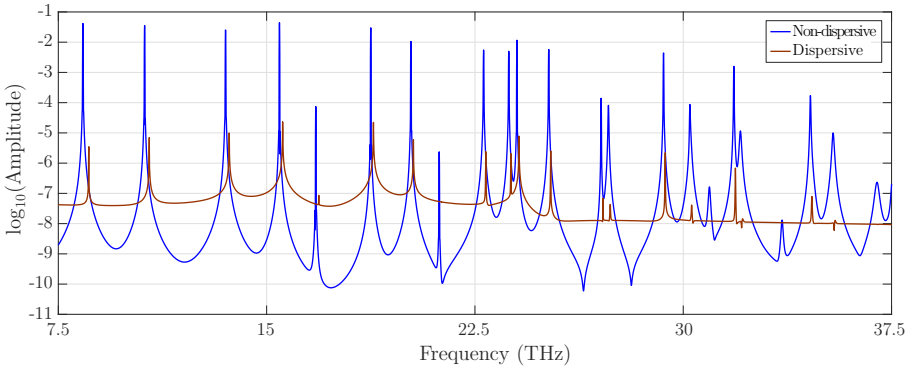

Figure 11: Rectangular cavity: Comparison of the computed spectra for non–dispersive and dispersive cavities.

In this numerical example, with a coarse mesh of 8×4 elements and a cubic degree of approximation, it is possible to capture resonant frequencies up to 22.49 THz with an error below 10^{-4} and resonant frequencies up to 31.48 THz with an error below 10^{-3}.

6.4. Three dimensional cavity

The final example considers a three dimensional PEC cavity of dimension $L \times L \times L$, where L=2μm filled with a non–dispersive material, for which an analytical solution is known [44]. The objective is to validate the implementation and illustrate the potential of the proposed approach in three dimensions.

The frequencies are computed using a series of structured hexahedral meshes with 2×2×2, 4×4×4, 8×8×8 and 16×16×16 elements and different degrees of approximation. Although the use of tetrahedral meshes is preferred for geometrically complex cavities, the use of hexahedral elements significantly reduces the cost of the time–domain solver due to the reduced number of interior faces compared to a tetrahedral mesh. The performance of different elements was studied in detail in [33], where it was concluded that, for domains that can be meshed with regular hexahedral elements, the accuracy level obtained with tetrahedral elements can be achieved using between 10 to 15 times less computational time using hexahedral elements.

Figure 12 shows the evolution of the error in two computed resonant frequencies as a function of the element size for a degree of approximation p ranging from 1 up to 3. The results demonstrate the optimal convergence properties of the proposed approach for computing the resonant frequencies in three dimensional cavities and illustrate, once more, the challenge of computing high resonant frequencies.

It is important to remark that the reduction in terms of number of degrees of freedom is more significant here than for the two dimensional problems discussed before. For instance, in order to obtain a relative error in the frequency f_9 below 10^{-5}, cubic elements employ a mesh with 64 elements (i.e, 24,576 degrees of freedom), quadratic elements require a mesh with 512 elements (i.e, 82,944

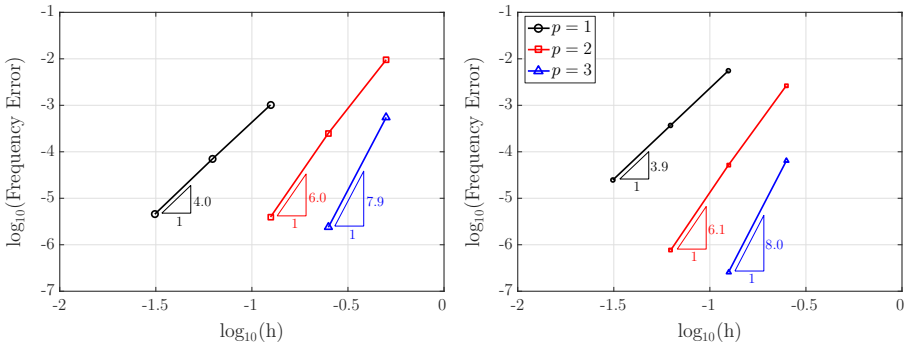

(a) $f_4 \approx 167.59$ THz (b) $f_9 \approx 248.57$ THz

Figure 12: Three dimensional cavity: h-convergence of the error for two resonant frequencies.

degrees of freedom) and linear elements require a further level of mesh refinement resulting in a mesh with 32,768 elements (i.e, 1,572,864 degrees of freedom). This means that cubic elements are able to perform a similar accuracy compared to linear elements by using 64 times less degrees of freedom.

In this numerical example, with a coarse mesh of 8×8×8 elements and a cubic degree of approximation, it is possible to capture resonant frequencies up to 509.66 THz with an error below 10^{-4} and resonant frequencies up to 749.50 THz with an error below 10^{-3}.

The resonant modes are again computed using another time–domain simulation as described in Section 5. Figure 13 shows the three components of the electric field for the resonant mode associated to the lowest frequency, $f_1 \approx 105.99$ THz.

To further illustrate the potential of the proposed methodology, Figure 14 shows the intensity of the electric and magnetic fields in four resonant modes, namely those associated with the resonant frequencies $f_4 \approx 167.59$ THz, $f_6 \approx 211.99$ THz, $f_{35} \approx 491.47$ THz and $f_{36} \approx 502.77$ THz.

All modes are computed on a mesh with only 64 hexahedral elements and using a degree of approximation $p = 3$. The relative error in the four resonant frequencies associated to the modes represented in Figure 14, ranges from 167.59 THz to 502.77 THz is below 10^{-5}.

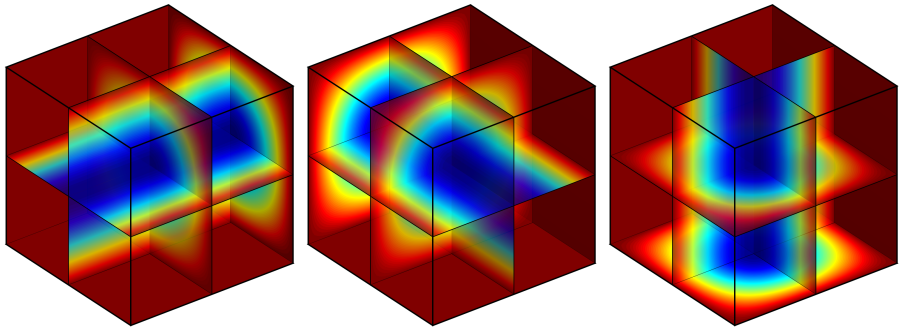

(a) E_1 (b) E_2 (c) E_3

Figure 13: Three dimensional cavity: three components of the electric field for the first resonant mode with frequency $f_1 \approx 105.99$ THz.

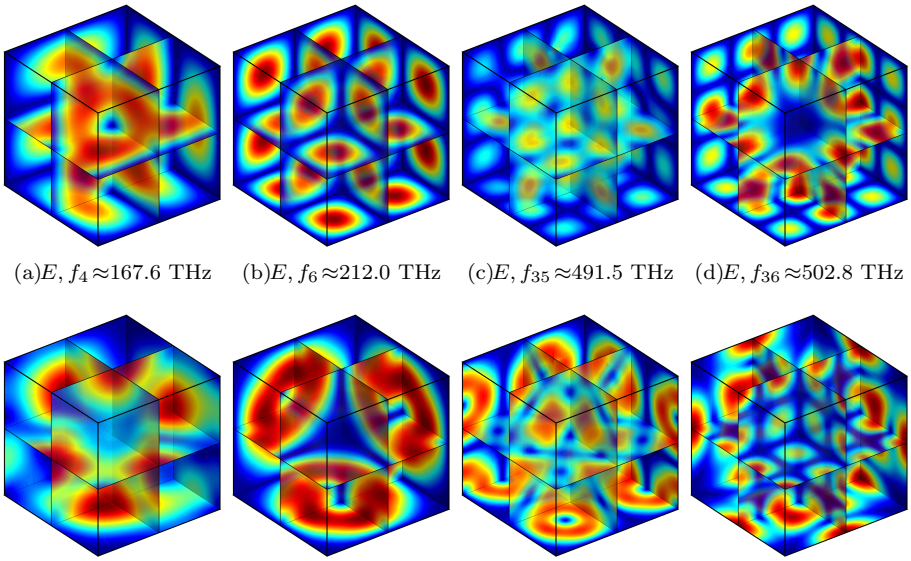

(a)E, $f_4 \approx$167.6 THz (b)E, $f_6 \approx$212.0 THz (c)E, $f_{35} \approx$491.5 THz (d)E, $f_{36} \approx$502.8 THz

(e)H, $f_4 \approx$167.6 THz (f)H, $f_6 \approx$212.0 THz (g)H, $f_{35} \approx$491.5 THz (h)H, $f_{36} \approx$502.8 THz

Figure 14: Three dimensional cavity: intensity of the electric (top) and magnetic (bottom) fields for four resonant modes.

7. Concluding remarks

The use of a high–order accurate DG solver for the computation of electromagnetic resonant frequencies and the associated modes in cavities has been described. The method is capable of incorporating the dispersive character

of frequency dependent materials using a single–pole Drude model. A unique capability of the proposed technique is the ability to incorporate the CAD representation of the boundary of the computational domain.

The optimal rate of convergence of the error of the computed frequencies has been numerically verified using two and three dimensional examples, involving cavities with curved boundaries and dispersive materials. The results show that the use of coarse meshes enables the efficient computation of the resonant frequencies and the coupling with an explicit time marching algorithm results in extremely low storage requirements, especially when compared to standard frequency domain methods. The results demonstrate that the traditional isoparametric finite element method does not achieve the optimal rate of convergence when cavities with curved boundaries are considered. This is shown to be related to the geometric approximation of curved boundaries. The NURBS–enhanced finite element method, which incorporates the exact description of the boundary, exhibits the expected optimal rate of convergence.

Acknowledgements

The authors gratefully acknowledge the financial support of the EPSRC Doctoral Training Grant (EP/J500318). The second author also gratefully acknowledges the financial support provided by the Sêr Cymru National Research Network for Advanced Engineering and Materials, United Kingdom.

References

[1] P. Arbenz, M. Bečka, R. Geus, U. Hetmaniuk, T. Mengotti, On a parallel multilevel preconditioned Maxwell eigensolver, Parallel Computing 32 (2006) 157–165.

[2] D. Boffi, Finite element approximation of eigenvalue problems, Acta Numerica 19 (2010) 1–120.

[3] O. Chinellato, P. Arbenz, M. Streiff, A. Witzig, Computation of optical modes in axisymmetric open cavity resonators, Future Generation Computer Systems 21 (2005) 1263–1274.

[4] R. Hiptmair, P. Ledger, Computation of resonant modes for axisymmetric Maxwell cavities using *hp*-version edge finite elements, International Journal for Numerical Methods in Engineering 62 (2005) 1652–1676.

[5] T.-M. Huang, W.-J. Chang, Y.-L. Huang, W.-W. Lin, W.-C. Wang, W. Wang, Preconditioning bandgap eigenvalue problems in three-dimensional photonic crystals simulations, Journal of Computational Physics 229 (2010) 8684–8703.

[6] S. Dey, R. Mittra, Efficient computation of resonant frequencies and quality factors of cavities via a combination of the finite-difference time-domain technique and the Padé approximation, Microwave and Guided Wave Letters, IEEE 8 (1998) 415–417.

[7] K. S. Yee, Numerical solution of initial boundary value problems involving Maxwell's equations in isotropic media, IEEE Transactions on Antennas and Propagation 14 (1966) 302–307.

[8] S. M. Rao, Time domain electromagnetics, Academic Press, 1999.

[9] J. S. Hesthaven, High–order accurate methods in time–domain computational electromagnetics: A review, Advances in Imaging and Electron Physics 127 (2003) 59–123.

[10] R. Sevilla, S. Fernández−Méndez, A. Huerta, Comparison of high–order curved finite elements, International Journal for Numerical Methods in Engineering 87 (2011) 719–734.

[11] R. Sevilla, S. Fernández−Méndez, A. Huerta, 3D NURBS–enhanced finite element method (NEFEM), International Journal for Numerical Methods in Engineering 88 (2011) 103–125.

[12] M. Ainsworth, Dispersive and dissipative behaviour of high order discontinuous Galerkin finite element methods, Journal of Computational Physics 198 (2004) 106–130.

[13] J. S. Hesthaven, T. Warburton, Nodal high–order methods on unstructured grids I. Time–domain solution of Maxwell's equations, Journal of Computational Physics 181 (2002) 186–221.

[14] B. Cockburn, F. Li, C.-W. Shu, Locally divergence–free discontinuous Galerkin methods for the Maxwell equations, Journal of Computational Physics 194 (2004) 588–610.

[15] T. Lu, P. W. Zhang, W. Cai, Discontinuous Galerkin methods for dispersive and lossy Maxwell's equations and PML boundary conditions, Journal of Computational Physics 200 (2004) 549–580.

[16] X. Ji, W. Cai, P. Zhang, High–order DGTD methods for dispersive Maxwell's equations and modelling of silver nanowire coupling, International Journal for Numerical Methods in Engineering 69 (2007) 308–325.

[17] M. König, K. Busch, J. Niegemann, The discontinuous Galerkin time–domain method for Maxwell's equations with anisotropic materials, Photonics Nanostruct. 8 (2010) 303–309.

[18] A. Taflove, A. Oskooi, S. G. Johnson, Advances in FDTD computational electrodynamics: photonics and nanotechnology, Artech house, 2013.

[19] T. Kashiwa, I. Fukai, A treatment by the FD-TD method of the dispersive characteristics associated with electronic polarization, Microwave and Optical Technology Letters 3 (1990) 203–205.

[20] M. Okoniewski, M. Mrozowski, M. Stuchly, Simple treatment of multi-term dispersion in FDTD, IEEE Microwave and Guided Wave Letters 7 (1997) 121–123.

[21] R. Luebbers, F. P. Hunsberger, K. S. Kunz, R. B. Standler, M. Schneider, A frequency-dependent finite-difference time-domain formulation for dispersive materials, Electromagnetic Compatibility, IEEE Transactions on 32 (1990) 222–227.

[22] D. F. Kelley, R. J. Luebbers, Piecewise linear recursive convolution for dispersive media using FDTD, IEEE Transactions on Antennas and Propagation 44 (1996) 792–797.

[23] D. M. Sullivan, Z-transform theory and the FDTD method, IEEE Transactions on Antennas and Propagation 44 (1996) 28–34.

[24] M.-H. Chen, B. Cockburn, F. Reitich, High–order RKDG methods for computational electromagnetics, Journal of Scientific Computing 22 (2005) 205–226.

[25] S. Lanteri, C. Scheid, Convergence of a discontinuous Galerkin scheme for the mixed time-domain Maxwell's equations in dispersive media, IMA Journal of Numerical Analysis 33 (2013) 432–459.

[26] R. Sevilla, S. Fernández−Méndez, A. Huerta, NURBS–Enhanced Finite Element Method (NEFEM): a seamless bridge between CAD and FEM, Archives of Computational Methods in Engineering 18 (2011) 441–484.

[27] R. Sevilla, S. Fernández−Méndez, A. Huerta, NURBS–enhanced finite element method (NEFEM), International Journal for Numerical Methods in Engineering 76 (2008) 56–83.

[28] R. Sevilla, S. Fernández-Méndez, Numerical integration over 2D NURBS shaped domains with applications to NURBS-enhanced FEM, Finite Elements in Analysis and Design 47 (2011) 1209–1220.

[29] O. C. Zienkiewicz, R. L. Taylor, The finite element method: the basis, volume 1, Butterworth-heinemann, 2000.

[30] R. Sevilla, S. Fernández-Méndez, A. Huerta, Nurbs-enhanced finite element method for Euler equations, International Journal for Numerical Methods in Fluids 57 (2008) 1051–1069.

[31] Q. Chen, I. Babuška, Approximate optimal points for polynomial interpolation of real functions in an interval and in a triangle, Computer Methods in Applied Mechanics and Engineering 128 (1995) 405–417.

[32] F. Witherden, P. Vincent, On the identification of symmetric quadrature rules for finite element methods, Computers & Mathematics with Applications 69 (2015) 1232 – 1241.

[33] R. Sevilla, O. Hassan, K. Morgan, The use of hybrid meshes to improve the efficiency of a discontinuous Galerkin method for the solution of Maxwellś equations, Computers & Structures 137 (2014) 2–13.

[34] H. L. Atkins, C. W. Shu, Quadrature–free implementation of discontinuous Galerkin method for hyperbolic equations, AIAA Journal 36 (1998) 775–782.

[35] Z. Q. Xie, R. Sevilla, O. Hassan, K. Morgan, The generation of arbitrary order curved meshes for 3D finite element analysis, Computational Mechanics 51 (2013) 361–374.

[36] R. Poya, R. Sevilla, A. J. Gil, A unified approach for a posteriori high-order curved mesh generation using solid mechanics, Computational Mechanics 58 (2016) 457–490.

[37] R. Sevilla, L. Rees, O. Hassan, The generation of triangular meshes for NURBS-enhanced FEM, International Journal for Numerical Methods in Engineering 108 (2016) 941–968.

[38] W.-H. Guo, W.-J. Li, Y.-Z. Huang, et al., Computation of resonant frequencies and quality factors of cavities by FDTD technique and Padé approximation, IEEE Microwave and Wireless Components Letters 11 (2001) 223–225.

[39] H. G. Dantanarayana, A. Vukovic, P. Sewell, T. M. Benson, Resonant frequency and q factor extraction from temporal responses of ultra-high q optical resonators, Science, Measurement & Technology, IET 8 (2014) 277–284.

[40] G. R. Werner, J. R. Cary, Extracting degenerate modes and frequencies from time-domain simulations with filter-diagonalization, Journal of Computational Physics 227 (2008) 5200–5214.

[41] V. Mandelshtam, FDM: the filter diagonalization method for data processing in NMR experiments, Progress in Nuclear Magnetic Resonance Spectroscopy 38 (2001) 159–196.

[42] G. Stark, M. Mishrikey, F. Robin, H. Jäckel, C. Hafner, R. Vahldieck, D. Erni, Positional dependence of FDTD mode detection in photonic crystal systems, International Journal of Numerical Modelling: Electronic Networks, Devices and Fields 22 (2009) 201–218.

[43] V. Madisetti, Digital signal processing fundamentals, CRC press, 2009.

[44] C. A. Balanis, Advanced Engineering Electromagnetics, John Wiley and Sons, New York, 1989.

[45] N. Kroll, The ADIGMA project, in: N. Kroll, H. Bieler, H. Deconinck, V. Couaillier, H. van der Ven, K. Sørensen (Eds.), ADIGMA – A European initiative on the development of adaptive higher–order variational methods for aerospace applications, volume 113 of *Notes on Numerical Fluid Mechanics and Multidisciplinary Design*, Springer, 2010, pp. 1–9.

[46] R. Sevilla, O. Hassan, K. Morgan, An analysis of the performance of a high-order stabilised finite element method for simulating compressible flows, Computer Methods in Applied Mechanics and Engineering 253 (2013) 15–27.